Numerical Study of Transonic Buffet on SC(2)-0518 and OAT15A with Vortex Generators

Yuta Tsukamoto* and Keiichi Kitamura†
Yokohama National University, Yokohama 240-8501, Japan

Predicting the transonic buffet and its onset is important for ascertaining the performance limits of an aircraft at its critical angle of attack. Additionally, a physical understanding of the buffet suppression technique is important for preventing shock wave oscillations. In this study, we conducted zonal detached-eddy simulations to numerically investigate the effects of vortex generators (VGs) on buffet suppression and to discuss the differing flow characteristics of the SC(2)-0518 and OAT15A supercritical airfoils when the chordwise position of the VGs is varied. The results for both airfoils equipped with VGs demonstrated significant suppression of large-scale lift oscillations across all calculation steps. VGs placed at 10% of the chord (10%c) from the leading edge produced higher time-averaged lift coefficients for both airfoils, with the OAT15A airfoil showing a particularly notable 2.5% improvement in lift coefficient, leading to a 0.82% increase in L/D ratio. The visualized results indicated that the interaction between the shock wave and VGs leads to variations in the separation point, depending on the VG chordwise position. This separation is affected by the aerodynamic characteristics of the airfoil shapes and the wake induced by the VGs, ultimately resulting in changes to the lift coefficient.

Nomenclature

AR	=	aspect ratio
A_v	=	vortex generator angle, °
a	=	speed of sound, m/s
C_L	=	lift coefficient
C_p	=	pressure coefficient
c	=	chord length, mm
D_v	=	vortex generator spacing distance, mm
d	=	distance from the wall, mm
e	=	wing thickness, mm
H_v	=	vortex generator height, mm
K	=	thermal conductivity constant
L	=	lift force, N
L_v	=	vortex generator length, mm
l	=	length scale or diagonal dimension
M	=	Mach number
P	=	static pressure, Pa
Pr	=	Prandtl number
q	=	dynamic pressure, Pa
Re	=	Reynolds number
S	=	surface area, m^2
T	=	temperature, K
t	=	time, s
U	=	freestream velocity, m/s
u	=	velocity in the x direction, m/s
W_v	=	vortex generator width, mm
X_v	=	vortex generator chordwise distance, mm
x	=	chordwise distance from leading edge, mm
y	=	spanwise distance from model center at leading edge, mm
z	=	distance normal to the chord line, mm
α	=	angle of attack, °
δ	=	Kronecker's delta
ε	=	tolerance
κ	=	von Karman constant, 0.41
μ	=	viscosity coefficient
ρ	=	density, kg/m^3
τ	=	stress tensor

Subscripts

ave	=	time-averaged
rms	=	root mean square
st	=	stagnation conditions
t	=	total or turbulent
∞	=	freestream conditions

I. Introduction

WHEN an aircraft reaches transonic flow conditions, the flow over the suction side of its wing can locally exceed Mach 1, given a certain combination of angle of attack and Mach number. This results in the formation of a shock wave over the wing. In such a situation, a large-scale boundary-layer separation induced by shock-wave/boundary-layer interactions can cause the shock wave to oscillate in the streamwise direction, a phenomenon typically known as the transonic buffet. This unsteady occurrence fluctuates the lift force on the wing owing to the unsteadiness of the flow separation. The primary vibrations caused by lift fluctuations range from 60 to 100 Hz with wind-tunnel scale airfoils [1–8], depending on the wing profile design and buffeting conditions. This low-frequency vibration may cause discomfort and unpleasantness for passengers, or it may also result in metal fatigue and structural damage to the aircraft, potentially leading to a severe aviation accident.

The transonic buffet was first observed experimentally by Hilton and Fowler in 1947 [9]; however, the complex physics governing this phenomenon remained unexplained for some time. Subsequent research has gradually shed light on the characteristics of the oscillating shock. Lee [1] proposed an acoustic wave-propagation feedback model for the mechanism underlying the self-oscillating shock, which is now a well-recognized model. Figure 1 illustrates Lee's feedback model. According to Lee's theory, pressure waves generated by the movement of the shock intensify as they propagate within the boundary layer. The interaction of the unsteady pressure waves at the trailing edge generates upstream pressure waves, which travel over the boundary layer on the upper wing surface and interact with the shock. The frequency at which the pressure waves produced at the shock travel to the trailing edge and return to the shock is defined as the shock-oscillating frequency.

Through subsequent experimental work with precise measurements, Jacquin et al. [2] observed self-sustaining large-scale shock
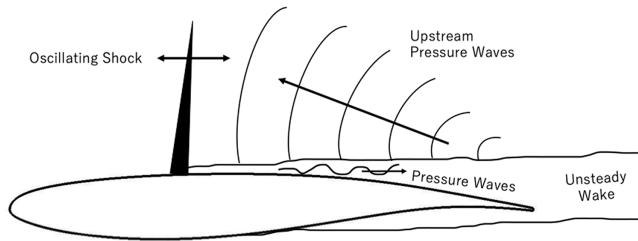
Fig. 1 Acoustic wave-propagation feedback model of self-sustained shock oscillation.

oscillations over the OAT15A supercritical wing profile at a buffet onset of Mach number $M = 0.73$ and angle of attack $\alpha = 3.5°$. In this work, the flowfield behavior was described in great detail through the precise characterization of the periodic motion by unsteady surface pressure measurements and high-speed schlieren visualization. The experimental results suggested that the transonic buffet is mediated by acoustic waves produced at the trailing edge, which then propagate along both sides of the airfoil, strongly supporting Lee's model.

Through numerical simulations of shock buffets using computational fluid dynamics, Crouch et al. [10] investigated the origins of transonic shock buffets through global stability analysis (GSA). Their results indicated that the global mode instability was the underlying mechanism for the transonic buffet. Using recent developments of GSA, Crouch et al. [11] analyzed the buffet on swept and unswept two-dimensional (2-D) wings, and the transition of stationary modes to unsteady traveling modes was shown on swept wings, contributing to more intricate buffeting-flow structures. Paladini et al. [12] investigated the differences between 2-D and three-dimensional (3-D) transonic buffet global modes and showed that the buffet frequency from the 3-D mode increases linearly with the sweep angle, explaining that this buffet frequency is much higher than that in two dimensions.

In a successive transonic buffet simulation, Moise et al. [13] employed large-eddy simulation (LES) to successfully capture the buffet characteristics with a supercritical airfoil. However, a previous study indicated that the accuracy of the numerical calculation is dictated by the accuracy of the turbulence model [14]. Using the unsteady Reynolds-averaged Navier–Stokes (URANS) model for transonic buffet simulations, an additional 1° of angle of attack was necessary compared to the experimental value [15]. Other models—including the original detached-eddy simulation (DES) and its variants, such as delayed DES (DDES)—failed to predict the shock-wave/boundary-layer interaction accurately in our preliminary simulations and in Ref. [16]. This inadequacy is due to the thickness of the Reynolds-averaged Navier–Stokes (RANS) region being insufficient to maintain a turbulent boundary layer until it interacts with the shock (calculation examples using DDES are described in Sec. II.B). This is because DES and its variants introduce significant dependence on the near-wall grid spacing in the tangential direction. The switch to the LES mode may occur inside the RANS boundary layer, leading to a "grid-induced separation" [17], as commented on transonic buffet simulations by Ehrle et al. in [18]. To sustain the attached boundary layer in the RANS region, Deck proposed a new hybrid RANS/LES switching method called Zonal DES [3]. In this method, the user can manually set the thickness of the RANS region so that the boundary layer is computed with full RANS behavior. Consequently, transonic buffet calculations using Zonal DES have succeeded in accurately reproducing the periodic motion of the shock without artificially increasing the angle of attack α to match experimental observations [3].

In terms of buffet suppression techniques, various flow control methods have been proposed. One such method to reenergize boundary layers and suppress flow separation is the use of vortex generators (VGs) [4,5,7,8]. It is well-established that a VG can control shock wave oscillation when installed on the upper surface of a wing. VGs are passive devices that generate longitudinal vortices over an airfoil surface in the direction of fluid flow. They promote the transition of the boundary layer over the object surface to a turbulent state, which is less susceptible to separation [4]. Moreover, the

mixing effect of the slower flow at the lower part of the boundary layer with the faster, uniform flow outside delays the separation point.

Blade-type VGs are often employed on aircraft wings and are named for their rectangular, blade-like shape [19]. A previous study by Takimoto [5] reported superior results, with an approximately 3% increase in the L/D ratio and buffet suppression for the SC(2)-0518 supercritical airfoil, using blade-type VGs positioned at 10% chord length (10%c) from the leading edge, compared to VGs placed at 20%c. However, Koike et al. [20] conducted a VG parametric study on the same airfoil and indicated that the most effective chordwise position for VG placement was at $x/c = 0.20$. Nevertheless, there is a paucity of convincing studies on the SC(2)-0518 airfoil to substantiate the general effectiveness of leading-edge VGs, warranting more detailed research to ascertain optimal VG positioning. Additionally, the studies that predicted effective VG placements focused solely on the SC(2)-0518 airfoil, which is not typically used in transonic buffet research. Another supercritical airfoil, OAT15A, is more commonly employed in both experimental and numerical transonic buffet studies. Although several studies have applied VGs on OAT15A, none have conducted a series of numerical predictions that represent shock wave buffet and suppression of shock wave oscillation across multiple airfoils. Our motivation is derived from this gap in the research.

Therefore, the objectives of this study are twofold: 1) to compare the characteristic differences of VGs on two different airfoil profiles, and 2) to examine the effects of VG positioning on these airfoils. In our work, numerical analyses are conducted for the SC(2)-0518 and OAT15A supercritical airfoils. We initially examine the nonbuffet cruising condition without VGs, followed by the buffet condition without VGs. Subsequently, the analysis incorporates scenarios with VGs attached during the buffeting condition. The VG placements are varied in two scenarios: VGs at $x/c = 0.10$ and 0.20.

II. Numerical Setup

A. Governing Equations

The governing equations are the 3-D compressible Navier–Stokes equations:

$$\frac{\partial \boldsymbol{Q}}{\partial t} + \frac{\partial \boldsymbol{F}_{e_j}}{\partial x_j} = \frac{1}{Re} \frac{\partial \boldsymbol{F}_{v_j}}{\partial x_j} \tag{1}$$

where

$$\boldsymbol{Q} = \begin{pmatrix} \rho \\ \rho u_j \\ e_T \end{pmatrix} \tag{2}$$

$$\boldsymbol{F}_e = \begin{pmatrix} \rho u_j \\ \rho u_i u_j + p\delta_{ij} \\ (e_T + p)u_j \end{pmatrix} \tag{3}$$

$$\boldsymbol{F}_v = \begin{pmatrix} 0 \\ \tau_{ij} \\ u_k \tau_{kj} + K \dfrac{\partial T}{\partial x_j} \end{pmatrix} \tag{4}$$

$$\tau_{ij} = \mu \left(\frac{\partial u_i}{\partial x_j} + \frac{\partial u_j}{\partial x_i} \right) - \frac{2}{3} \mu \frac{\partial u_k}{\partial x_k} \delta_{ij} \tag{5}$$

Subscripts i, j, and k assume values of 1, 2, and 3, denoting the Cartesian coordinates, and all quantities are dimensionless. The working gas is air, approximated by the calorically perfect gas model with the specific heat ratio $\gamma = 1.4$. The nondimensionalized molecular viscosity coefficient μ is calculated from Sutherland's law. The nondimensionalized thermal conductivity coefficient K is obtained from $K = \mu$, assuming that the Prandtl number is constant

with $Pr = 0.71$. To model turbulence, the molecular viscosity is replaced by $(\mu + \mu_t)$, where μ_t is the turbulence viscosity given by the turbulence model. Similarly, the thermal conductivity κ is replaced by $(\mu + \mu_t Pr/Pr_t)$, where the turbulent Prandtl number $Pr_t = 0.90$.

B. Numerical Methods

We used the FaST Aerodynamic Routines (FaSTAR) code developed by the Japan Aerospace Exploration Agency (JAXA) as our fluid solver [21]. The numerical methods employed are as delineated in the previous study by Hashimoto et al. [22]. To discretize the governing 3-D compressible Navier–Stokes equations aforementioned, we applied the cell-centered finite volume method. To achieve second-order spatial accuracy, monotone upstream-centered schemes for conservation laws (MUSCL) interpolation [23] was used. For the computation of the numerical Euler flux, the simple low-dissipation advection upstream splitting method (SLAU) scheme [24] was employed. Gradient reconstruction was performed using the Green–Gauss-based weighted least squares method (GLSQ) approach [25], and Hishida (van Leer type) [26] was adopted as the slope limiter. Time integration was facilitated through the lower–upper symmetric Gauss–Seidel (LU-SGS)-type implicit method [27] coupled with a second-order accurate dual time-stepping approach, as detailed in [28].

In the present work, we implemented the Zonal DES method as our turbulence model, which is a hybrid RANS/LES approach proposed by Deck [3]. This method was chosen for its efficiency over the wall-modeled LES (WMLES) model, particularly in handling complex geometries [29], such as VG-mounted airfoils. For the RANS portion of the simulations, we used the one-equation Spalart–Allmaras turbulence model without the f_{t2} tripping term (SA-noft2). To elucidate our selection of the Zonal DES method for transonic buffet simulations, a concise overview of the Spalart–Allmaras turbulence model and the DES technique is provided.

1. Spalart–Allmaras RANS Turbulence Model

The one-equation Spalart–Allmaras model computes the working variable $\tilde{\nu}$ based on the concept of turbulent viscosity. Note that $\tilde{\nu}$ is governed by the following equation:

$$\frac{D\tilde{\nu}}{Dt} = c_{b1}\tilde{S}\tilde{\nu} + \frac{1}{\sigma}[\nabla((\nu + \tilde{\nu})\nabla\tilde{\nu}) + C_{b2}(\nabla\tilde{\nu})^2] - c_{w1}f_w\left(\frac{\tilde{\nu}}{d}\right)^2 \quad (6)$$

The turbulent eddy viscosity is determined by

$$\mu_t = \rho\tilde{\nu}f_{v1} \quad (7)$$

where

$$f_{v1} = \frac{\chi^3}{\chi^3 + c_{v1}^3}, \quad \chi = \frac{\tilde{\nu}}{\nu} \quad (8)$$

In the production term,

$$\tilde{S} \equiv S + \frac{\tilde{\nu}}{\kappa^2 d^2}f_{v2} \quad (9)$$

where

$$S = \sqrt{2S_{ij}S_{ij}}, \quad S_{ij} = \frac{1}{2}\left(\frac{\partial u_i}{\partial x_j} - \frac{\partial u_j}{\partial x_i}\right), \quad f_{v2} = 1 - \frac{\chi}{1 + \chi f_{v1}} \quad (10)$$

and d represents the distance to the wall. The modified strain rate $\tilde{S}$ ensures the maintenance of log-layer behavior ($\tilde{S} = \mu_\tau/\kappa d$) all the way to the wall, given that the eddy viscosity ν_t equals $\kappa y\mu_\tau$ within the log layer and differs in the buffer layer and the viscous sublayer.

Originally, the Spalart–Allmaras model included a destructive term [the last term on the right-hand side of Eq. (6)], $-c_{w1}(\tilde{\nu}/d)^2$.

Numerical tests indicated that with this term, the model significantly underestimated the skin friction coefficient for flat plate boundary layers [34]. To enhance the decay of the destruction term in the outer region of the boundary layer, a calibration factor f_w was introduced and applied to the destructive term:

$$\begin{cases} f_w = g\left[\dfrac{1+c_{w3}^6}{g^6 + c_{w3}^6}\right]^{1/6} \\ g = r + c_{w2}(r^6 - r) \end{cases} \quad (11)$$

where

$$r \equiv \frac{\tilde{\nu}}{S\kappa^2 d^2} \quad (12)$$

Both r and f_w are designed to equal 1 in the log layer and to decrease in the outer region of the boundary layer. The model constants are as follows:

$$\begin{aligned} c_{b1} &= 0.1355, \quad c_{b2} = 0.622, c_{v1} = 7.1, \\ c_{w1} &= \frac{c_{b1}}{\kappa^2} + \frac{1 + c_{b2}}{\sigma}, \quad c_{w2} = 0.3, \quad c_{w3} = 2.0, \\ \sigma &= 2/3, \quad \kappa = 0.41 \end{aligned} \quad (13)$$

2. DDES and Zonal DES

In the general DDES framework, the wall distance d is replaced with the length scale of DDES: l_{DDES}. l_{DDES} is expressed as follows [30]:

$$l_{DDES} = d - f_d \max(0, d - C_{DES}\Delta) \quad (14)$$

Here, C_{DES} is the model constant, which is set to 0.65 as calibrated by Shur et al. [31]. The grid scale Δ is given by

$$\Delta = \min[\max\{c_w d, 2c_w\Delta_{max}, 2\Delta_{wn}\}, 2\Delta_{max}] \quad (15)$$

where Δ_{max} is the largest distance from the cell-face to cell-center, Δ_{wn} is one half of the grid scales in the direction normal to the wall surface, and c_w is the model constant, which is 0.15 in FaSTAR [31]. Additional functions are defined as follows:

$$f_d = 1 - \tanh[(8r_d)^3], \quad r_d = \frac{\nu_t + \nu}{S_d\kappa^2 d^2}, \quad S_d = \sqrt{\frac{\partial u_i}{\partial x_j}\frac{\partial u_i}{\partial x_j}} \quad (16)$$

The use of DDES was insufficient for capturing the transonic buffet, as previously mentioned in the Introduction. Specifically, our initial computations with DDES failed to produce an accurate representation of the shock-oscillating motion over the OAT15A airfoil, corroborating the concerns outlined in [18]. Figure 2 illustrates the issue with the DDES calculations. The root mean square (RMS) field of the velocity fluctuations demonstrates that the highlighted region differs from experimental results; notably, DDES predicts oscillations occurring further upstream. The boundary-layer attachment appears weak from the leading edge, which results in the shock wave tracing back to $x/c \sim 0.17$, in contrast to $x/c \sim 0.4$, as reported in the previous study [2].

In contrast to DDES, the RANS region in the Zonal DES method can be manually defined by the user. Computations are performed using the RANS model within the specified region and the LES model outside of it. Specifically, the wall distance d is replaced with the length scale of Zonal DES: l_{ZDES}, where the mode switching of the RANS and LES length scale is defined by

$$l_{ZDES} = \begin{cases} l_{RANS} & \text{if } d \leq d_{input} \\ l_{LES} & \text{if } d \geq d_{input} \end{cases} \quad (17)$$
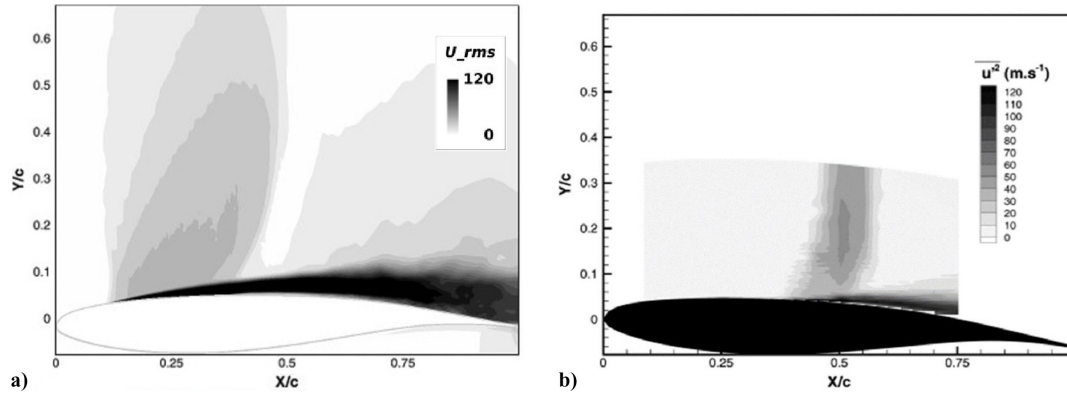
Fig. 2   RMS fields of chordwise velocity fluctuation over the OAT15A airfoil: a) results from the DDES calculation and b) experimental results [3] (taken with permission by AIAA).

where l_{RANS} is the length scale of RANS (i.e., $l_{RANS} = d$), l_{LES} is the length scale of LES ($l_{LES} = C_{DES}\Delta$), and d_{input} is the wall distance set by the user. Figure 3 presents the model switching region with the user-defined d_{input}. In our research, d_{input} was chosen as 1.5 times the boundary-layer height at the shock position under cruising conditions. The location of the RANS/LES hybrid interface remains a subject of discussion, as indicated in [32,33], with no definitive guidelines for shock-induced, separated boundary layers, such as those encountered in transonic buffeting flows. Hence, the RANS region thickness in this study was determined based on the methodology adopted by Ishida et al. [30]. For our purposes, this corresponds to a thickness of 3.0 mm for both the SC(2)-0518 and OAT15A profiles. The RANS model employed is the SA-noft2 [34], as discussed earlier. The number of inner iterations was set to four, with the local Courant–Friedrichs–Lewy (CFL) numbers being 60 (SC(2)-0518) and 130 (OAT15A) near the wall, and the time step was fixed at $dt = 0.05$ in dimensionless time. Some studies argued that RANS and LES should be switched rapidly [as in Eq. (17) or in [35,36]] or continuously by a blending function [32,33]. In our calculations, we did not use a blending function at the interface of two modeling zones. In terms of the numerical discontinuity shown in Eq. (17), we have verified that no numerical discontinuity was generated at the RANS/LES interface from our preliminary calculations using the aforementioned interface settings. Figure 4 shows the instantaneous

Mach number contour near the interface (in dashed lines), revealing no spurious numerical noise generated at the interface.

C.   SC(2)-0518 and OAT15A Supercritical Airfoil Characteristics

In this study, we compared the transonic buffet characteristics of the SC(2)-0518 and OAT15A supercritical airfoils to gain insights into the differences in buffeting and the VG placement effects. SC(2)-0518 is designed to provide higher lift coefficients at lower Mach numbers [37]; however, it tends to be excessively thick for transonic flights (resulting in higher drag). In contrast, OAT15A offers lower drag while maintaining sufficient lift (demonstrated later in this paper) in the transonic region.

The SC(2)-0518 supercritical airfoil has a chord length of $c = 200$ mm, a maximum thickness-to-chord ratio $e/c = 18.0\%$, and a blunt trailing edge representing 0.69% of the chord length. At a freestream Mach number $M = 0.70$ and Reynolds number (based on the freestream velocity and chord length) $Re = 5.0 \times 10^6$, the buffet onset occurred at an angle of attack α exceeding 3.8°. The primary buffet frequency was approximately 80 Hz at $\alpha = 3.8°$ and increased to 95 Hz at $\alpha = 4.9°$. For further details on the experiment, refer to Yamaguchi et al. [6] and Koike et al. [20].

For the OAT15A wing model experiment, the chord length is $c = 230$ mm, with a maximum thickness-to-chord ratio $e/c = 12.5\%$ and a blunt trailing edge comprising 0.50% of the chord
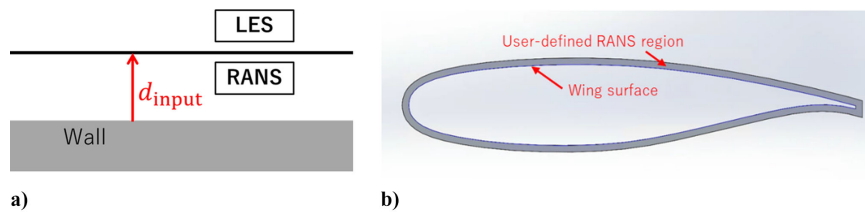

Fig. 3   Zonal DES switching theory: a) schematic showing the RANS/LES switching distance as defined by the user and b) depiction of the RANS region around the airfoil.
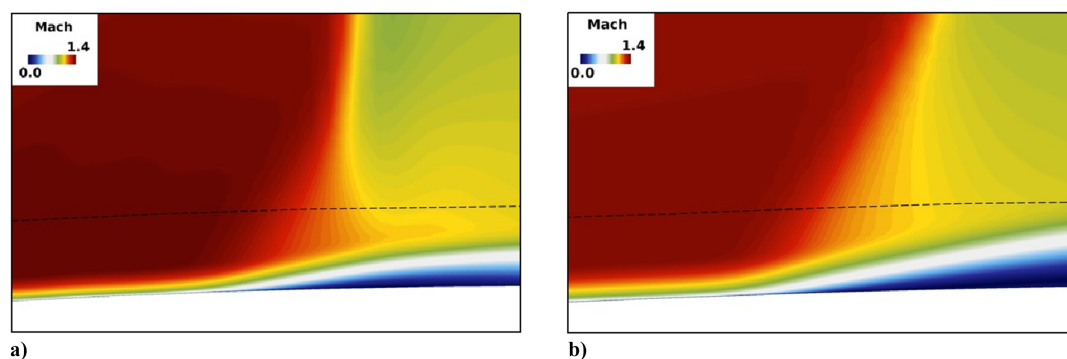

Fig. 4   Instantaneous Mach number contour around the RANS/LES interface (dashed line) at shock-foot, visualized at the 200,000th calculation step: a) SC(2)-0518 airfoil and b) OAT15A airfoil, both under buffet conditions.

length. The buffet onset was observed when the angle of attack surpassed $\alpha = 3.25°$, with a freestream Mach number $M = 0.73$ and Reynolds number (based on the freestream velocity and chord length) $Re = 3.0 \times 10^6$. The main buffet frequency was observed to be around 70 Hz, consistently across different angles of attack. Jacquin et al. [2] provided a detailed account of this experiment.

D. Vortex Generator Parameters

The setup parameters for the VG are discussed in this section. For our study, a blade-type VG was used [19]. The blade-type VG, having a rectangular shape, enables straightforward parameterization. We adopted the baseline parameters from Koike et al. [20]. Figure 5 illustrates an overview of the VG. The VG parameters are as follows: VG height $H_v = 6.0 \times 10^{-3}\, c$, VG length $L_v = 2.4 \times 10^{-2}\, c$ (aspect ratio $AR = L_v/H_v = 4$), VG width $W_v = 5.0 \times 10^{-4}\, c$, VG spacing $D_v = 0.24\, c$, and VG attachment angle $A_v = 20°$. The chordwise VG positions considered were $X_v = 0.10\, c$ and $0.20\, c$.

E. Grids

In this study, we created two types of grids using O-topology: a set of 2-D grids with three grid densities (coarse, medium, and fine grids) and a set of 3-D grids obtained by extruding the 2-D grids in the spanwise direction. Table 1 presents the grids used in each section. These two types of grids were employed to verify the grid convergence and to validate the numerical methods with experimental results through two stages of calculations. In the first stage, a grid convergence study was conducted using 2-D grids with three different grid densities. The calculations were carried out under nonbuffet cruising conditions at low angles of attack. In the second stage, numerical validation was performed by comparison with experimental results under buffeting conditions. These two stages of calculations are essential to perform the verification and validation of our computational approach.

The following grids for each airfoil were generated using Pointwise [38]. An O-topology structured mesh was employed for this study. The grid details are depicted in Fig. 6 (detailed cell numbers for

each case will be introduced in Sec. III.A). The wing model is centered within the grid, and the far-field diameter is set to $60c$ (60 times the chord length c). The near-wall grid spacing is set at $3.0 \times 10^{-6}\, c$ (SC(2)-0518) and $4.3 \times 10^{-6}\, c$ (OAT15A), ensuring $y^+ < 1$. These spacings also fulfill the grid density requirements of hybrid RANS/LES in all directions, i.e., $\Delta x^+ < 600$ (streamwise), $\Delta y^+ < 1$, and $\Delta z^+ < 300$ (spanwise) [29]. These 2-D grids are used for nonbuffeting, VG-less conditions for the grid convergence study. The 3-D grids for buffeting or VG-on conditions employ periodic boundary conditions to economize computational resources. We set the spanwise domain to match the VG spacing intervals, and periodic boundary conditions are implemented between the port and starboard sidewalls, simulating a setup with multiple VGs in place. The spanwise domain (i.e., VG spacing D_v) is set to $0.24c$, which is 48 mm (SC(2)-0518) and 55.2 mm (OAT15A), to match the baseline conditions employed from the corresponding VG study [20]. Thus, the number of VGs across the span is one. The spanwise grid points for the 3-D grids are set to 121 (SC(2)-0518) and 122 (OAT15A).

III. Verifications and Validations (Without VGs)

A. Grid Convergence Study

The calculation grids were verified with three 2-D grids of different densities (i.e., coarse, medium, and fine grids) under nonbuffet conditions. The calculations were carried out using low-cost, steady RANS (SA-noft2) computations. Zonal DES was not employed in this nonbuffet case owing to the steady nature of the flow. However, it was confirmed that the Zonal DES calculations also exhibited no buffet phenomenon.

Initially, the verification was conducted on the SC(2)-0518 airfoil using three grids: coarse, medium, and fine. The numbers of grid points for the upper and lower wing surfaces, the blunt trailing edges, and the total cell numbers generated are shown in Table 2. The number of grid points in the wall-normal direction was 144. With these grids, the flow around the SC(2)-0518 airfoil was numerically calculated at a cruise condition of $M = 0.70$ and $\alpha = 2.5°$. The pressure coefficient distribution is shown in Fig. 7a. The results
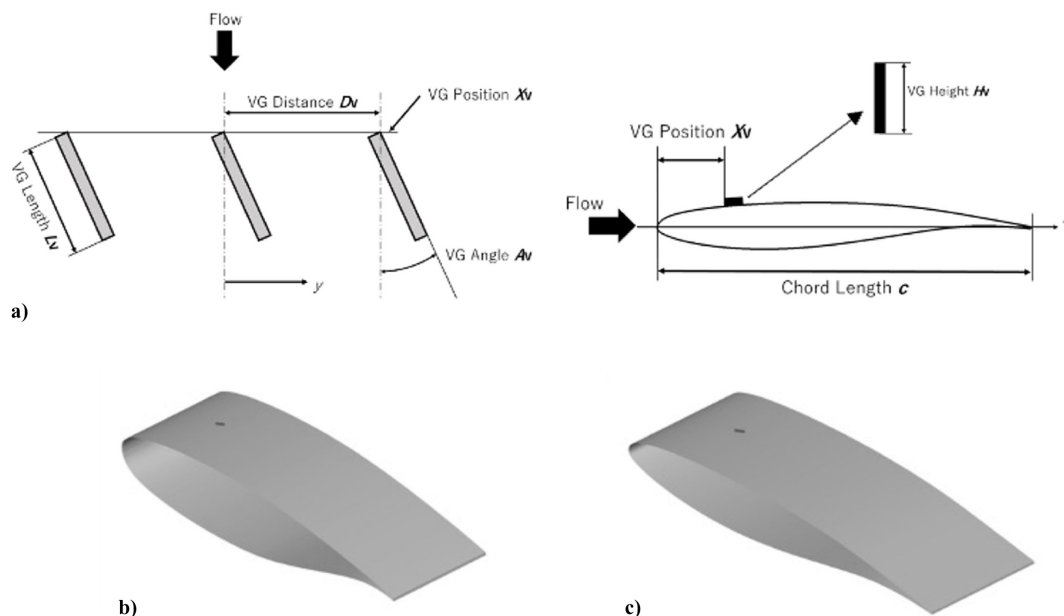

Fig. 5 VG parameter definitions and overview of a representative VG-attached case: a) VG parameters, b) VG on SC(2)-0518, and c) VG on OAT15A.

Table 1 Grid variations

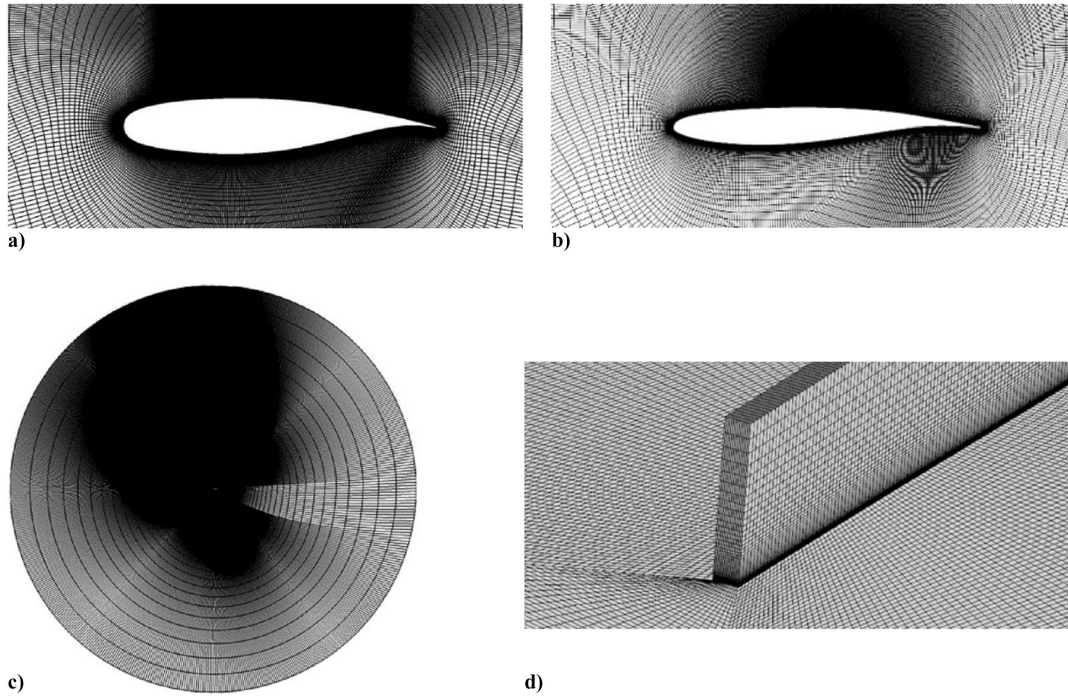| Grids in section	2-D/3-D	Flow conditions	VGs	Grid density	Turbulence modeling
III.A	2-D	Cruising	No	Coarse, medium, fine	RANS
III.B	3-D	Cruising/buffeting	No	Medium	Zonal DES
IV	3-D	Buffeting	Yes	Medium	Zonal DES

Fig. 6   Computational meshes a) mesh around the SC(2)-0518 airfoil, b) mesh around the OAT15A airfoil, c) overview of the O-topology mesh, and d) close-up view of the mesh at the leading edge of a VG.

Table 2   SC(2)-0518 grid density verification

SC(2)-0518	Upper + lower + trailing edges	No. of cells
Coarse	325 + 140 + 10	67,496
Medium	650 + 280 + 20	135,421
Fine	1,300 + 560 + 40	271,271

Table 3   OAT15A grid density verification

OAT15A	Upper + lower + trailing edges	No. of cells
Coarse	290 + 115 + 4	56,434
Medium	575 + 230 + 8	112,590
Fine	1,150 + 460 + 16	225,597

indicated only minor differences between the three grid densities, confirming that the calculation accuracy is independent of the grid density. Therefore, the medium grid was chosen for subsequent SC(2)-0518 airfoil calculations.

Subsequently, the OAT15A airfoil was also numerically analyzed at a cruise condition of $M = 0.73$ and $\alpha = 2.5°$, with three different grid densities, as detailed in Table 3. The number of grid points in the wall-normal direction was 140. Figure 7b shows its C_p distributions. The results showed similar distributions, with negligible differences between them. Based on grid convergence, the medium grid was chosen for OAT15A calculations.

B.   Transonic Buffet Simulation

The same two airfoils were analyzed at buffet conditions of $M = 0.70$ and $\alpha = 3.8°$ for SC(2)-0518 and $M = 0.73$ and $\alpha = 3.5°$ for OAT15A. For the buffet condition calculations, a 3-D grid based on the 2-D medium grid described in III.A. was employed, extending into the spanwise direction. SC(2)-0518 had 121 spanwise (y-direction) grid points, whereas OAT15A had 122.

1.   SC(2)-0518 Airfoil

The SC(2)-0518 case was computed at a buffet condition of $M = 0.70$ and $\alpha = 3.8°$. Self-sustaining shock oscillations are noted from
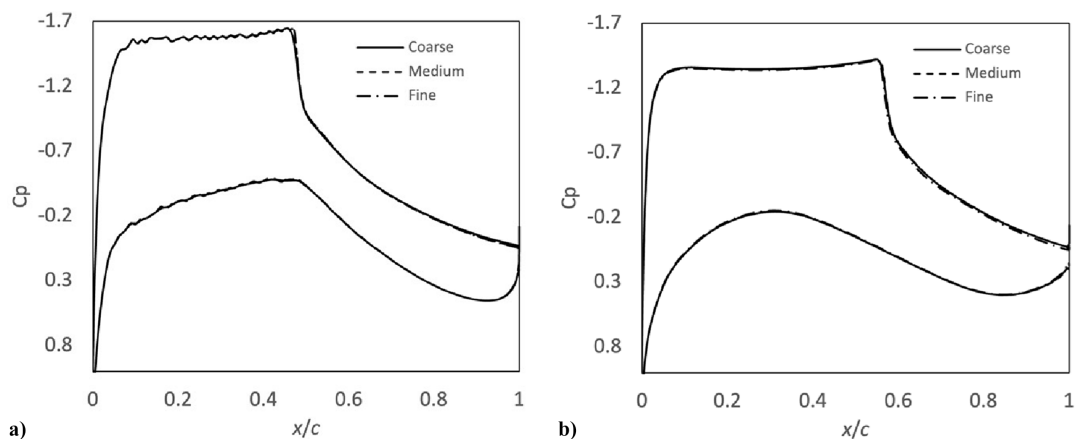

Fig. 7   Pressure coefficient distribution around a) the SC(2)-0518 airfoil at a cruise condition of $M = 0.70$ and $\alpha = 2.5°$ and b) the OAT15A airfoil at a cruise condition of $M = 0.73$ and $\alpha = 2.5°$ for grid convergence.

the visualized results. The pressure coefficient distribution over the wing surface is illustrated in Fig. 8a, representing time-averaged values across three periods preceding the calculation conclusion. Minor deviations are observed from the leading edge to the trailing edge on both sides of the airfoils—notably underestimating C_p near the trailing edge ($0.70 < x/c < 1.0$). This discrepancy occurs within the region characterized by unsteady and complex, separated flow. Figure 9 illustrates the RMS values of pressure fluctuations extracted from the same computational step as the averaged C_p distribution depicted in Fig. 8. The highlighted pink region in Fig. 9a indicates a notably high-pressure fluctuation, particularly evident at the trailing edge. This phenomenon is attributable to the separated flow at the shock-foot location. The separated flow near the wing surface contributes to a partial re-attachment at the trailing edge, resulting in a relatively low-pressure surface—and consequently an underestimated C_p distribution. Our analysis results indicate that the computational results demonstrate sufficiently accurate pressure distributions, aligning well with the experimental values and overall trend. Figure 10 exhibits the time history of the lift coefficient, revealing the variability in lift force due to the unsteady flow separation. The shock induces flow separation at the shock-foot location, and as the shock oscillates, the separation point oscillates, resulting in periodic changes in the low-pressure region atop the wing (i.e., the lift force fluctuates); this represents the basic principle of the transonic shock buffet phenomenon. Table 4 details the main buffet frequency f averaged over three cycles before the end of the simulation. The deviation in vibration frequency from the experimental data is only 0.3%, indicating excellent alignment with both the average pressure coefficient and the vibration frequency.

2. OAT15A Airfoil

The numerical buffet simulation for OAT15A was conducted at $M = 0.73$ and $\alpha = 3.5°$. Periodic shock oscillations were observed. Figure 8b shows the pressure coefficient distributions, time-averaged over three oscillation periods. Although C_p exhibits a minor increase on
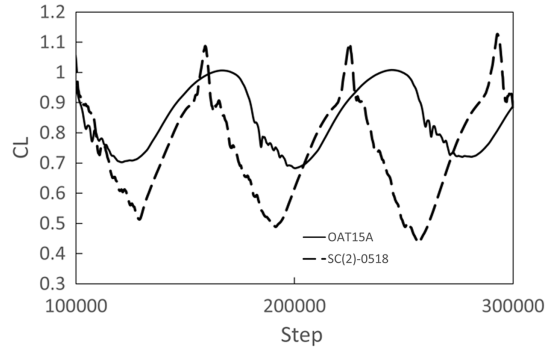

Fig. 10   Lift coefficient time history at buffet condition.

Table 4   Main buffet frequency measured over each airfoil

Airfoil	CFD	Experiment
SC(2)-0518	80.5 Hz	80.3 Hz [6]
OAT15A	65.3 Hz	69 Hz [2]

the upper side of the wing, the plateau within $0.05 < x/c < 0.35$ and the shock position in the range of $0.35 < x/c < 0.55$ are accurately represented, with the overall distribution aligning closely with experimental results. The plateau represents the supersonic region preceding the shock, indicative of supercritical airfoil designs that maintain a flattened aspect to postpone the onset of the shock. The flat design provides a gradual deceleration of the supersonic flow from near the leading edge to the shockwave front; this leads to a decreased Mach number before the shock, thus diminishing the shock strength [37]. Figure 11 illustrates the chordwise (x-direction) velocity fluctuations in the RMS field, displaying the shock chordwise displacement in
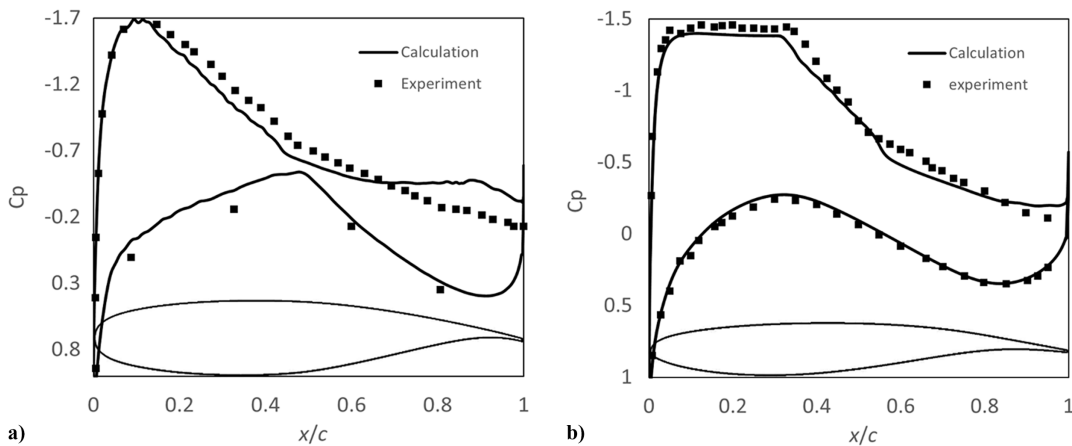

Fig. 8   Time-averaged pressure coefficient distribution around a) the SC(2)-0518 airfoil at buffet condition of $M = 0.70$ and $\alpha = 3.8°$ and b) the OAT15A airfoil at buffet condition of $M = 0.73$ and $\alpha = 3.5°$.
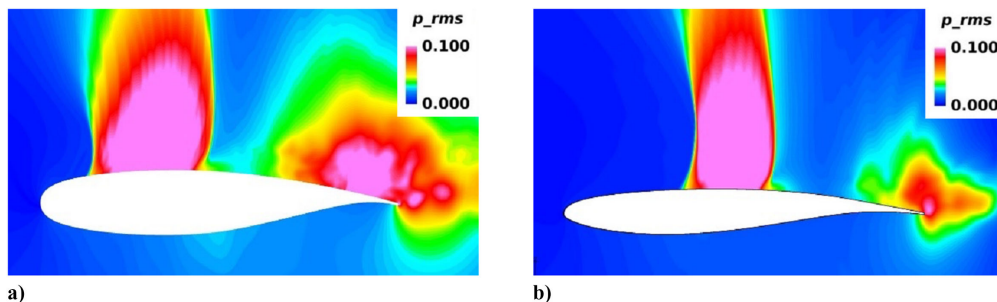

Fig. 9   RMS fields of pressure fluctuation at the cross section $y = 0$. a) The SC(2)-0518 airfoil at buffet condition of $M = 0.70$ and $\alpha = 3.8°$ and b) the OAT15A airfoil at buffet condition of $M = 0.73$ and $\alpha = 3.5°$.
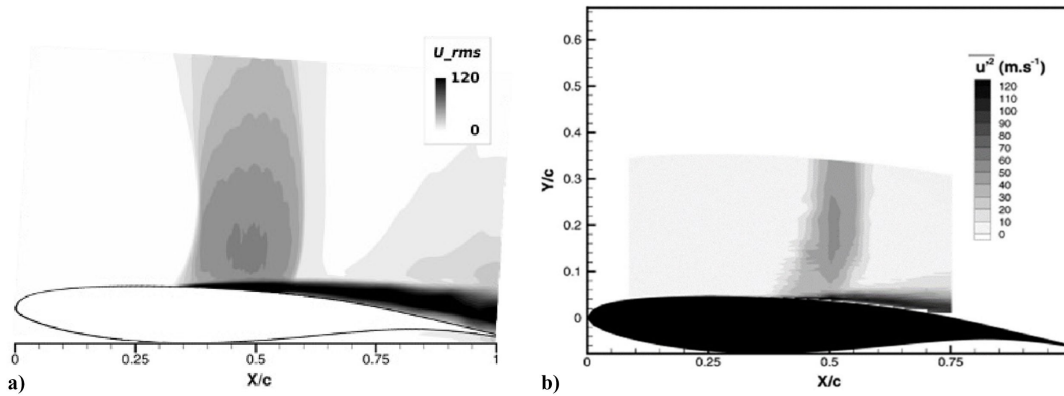
Fig. 11   RMS fields of chordwise velocity fluctuation over OAT15A airfoil: a) Zonal DES calculations from our study and b) experimental visualization [3] (taken with permission by AIAA).

grayscale. The simulations exhibit broader oscillations and darker shading near the shock-foot region, suggesting a more pronounced capture of the shock wave in the numerical model [3]. Table 4 presents the vibration frequency f averaged over three cycles before concluding the calculations, with only a 5% deviation from experimental frequency values.

The investigations based on the Zonal DES methodology and involving both SC(2)-0518 and OAT15A airfoils yielded reasonable consistency with experimental data under cruising and buffet conditions. This outcome validates the accuracy of our numerical setup for capturing the unsteady aerodynamic phenomena over the wings. With these confirmed grid dimensions, grids were established for the configurations with VGs, as shown in Fig. 6d. The VG regions were constructed with a structured mesh, maintaining y^+ values below 1. To accommodate a denser mesh near the VGs, an interpolation line was integrated, enhancing the mesh resolution through increased cell points. The cell count for grids with VGs exceeded those without VGs by approximately 2 million cells. The y-coordinate was defined with $y = 0$ at the tip of the VG. The total number of grid points for VG-equipped configurations was 18.2 million for SC(2)-0518 and 16 million for OAT15A.

IV.   Results with VGs

The effects of VGs and their variation with the chord length position ($10\%c$ and $20\%c$) will be discussed in terms of the time history of the C_L, C_p around the airfoil, the RMS field of the pressure fluctuation (P_{rms}), surface P_{rms} around the airfoil, and visualization by the Q criterion and Mach isosurfaces. Each case was run for 300,000 steps, with data storage occurring every 2000 steps. The time-averaged fields in the VG-equipped cases were averaged over steps ranging from 100,000 to 300,000. The averaged values are denoted with the subscript "ave."

A.   Lift Coefficients

Figure 12 illustrates the time histories of the C_L for each case with VGs installed. For comparative analysis, the C_L history for the scenario *without* VGs is also included, depicted as a dashed line. Figure 12a presents the C_L history with VGs on the SC(2)-0518 airfoil; the blue line represents the case with VGs positioned at $10\%c$, and the red line corresponds to the $20\%c$ placement. The cases with VGs demonstrated significant suppression of the large-scale lift oscillations across the entire range of calculation steps. The VG-equipped scenarios yielded smaller fluctuations in C_L, ranging from 0.75 to 1.0, whereas the cases without VGs exhibited fluctuations from 0.50 to 1.1. The average values resulted in a C_{Lave} of 0.874 for the VG at the $10\%c$ position and a C_{Lave} of 0.872 for the VG at $20\%c$ position, with a negligible difference of approximately 0.23%. Hence, no marked improvement was observed in C_L variability by altering the VG chord length position, at least at the $10\%c$ and $20\%c$ positions on the SC(2)-0518 airfoil.

Similarly, Fig. 12b shows the C_L history for the VG-equipped OAT15A airfoil. Large lift oscillations were significantly dampened
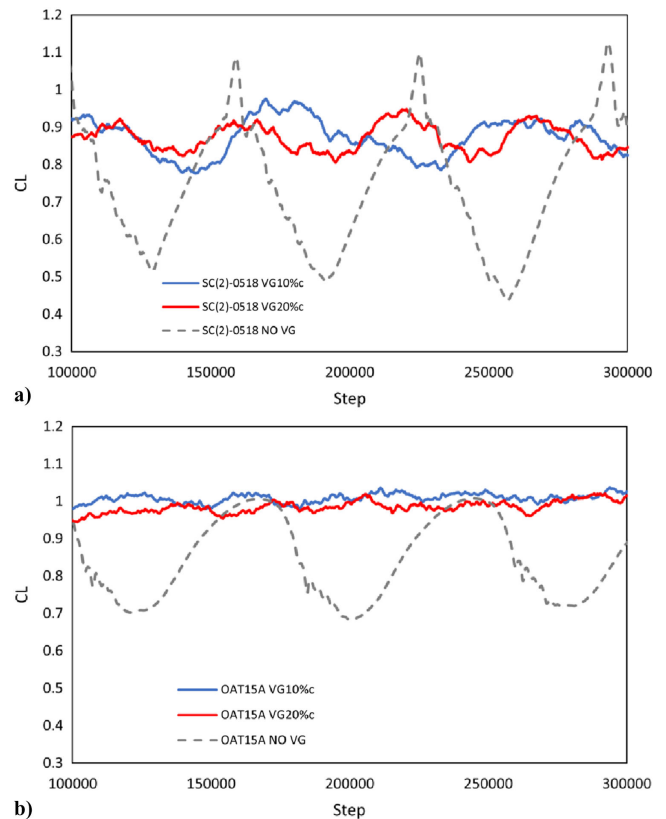

Fig. 12   Lift coefficient time history for VG-equipped cases: a) C_L history for the SC(2)-0518 airfoil and b) C_L history for the OAT15A airfoil. For comparison, the C_L history for cases without VGs is represented with dashed lines.

in both the $10\%c$ and $20\%c$ VG scenarios, leaving only minor lift fluctuations. Compared to the SC(2)-0518 airfoil, the VGs on OAT15A achieved a more stable suppression of lift oscillations. While the SC(2)-0518 airfoil with VGs exhibited some fluctuation within a C_L range of 0.75–1.0, the VGs on the OAT15A airfoil restricted the variation to a narrower band of 0.95–1.05. The averaged C_L was $C_{\mathrm{Lave}} = 1.01$ for the $10\%c$ VG case and $C_{\mathrm{Lave}} = 0.985$ for the $20\%c$ case, reflecting an improvement of approximately 2.5% for the $10\%c$ placement compared to the $20\%c$ case.

B.   Drag Coefficients

The drag coefficient C_D is also an important factor for discussing practical applications. Figure 13 shows the time histories of C_D for each case with VGs. For comparison, VG-less cases are also shown in dashed lines. Figure 13a represents the SC(2)-0518 cases, where the blue line represents the $10\%c$ VG-attached case and the red line represents the $20\%c$ attached case. The results reveal a suppression of
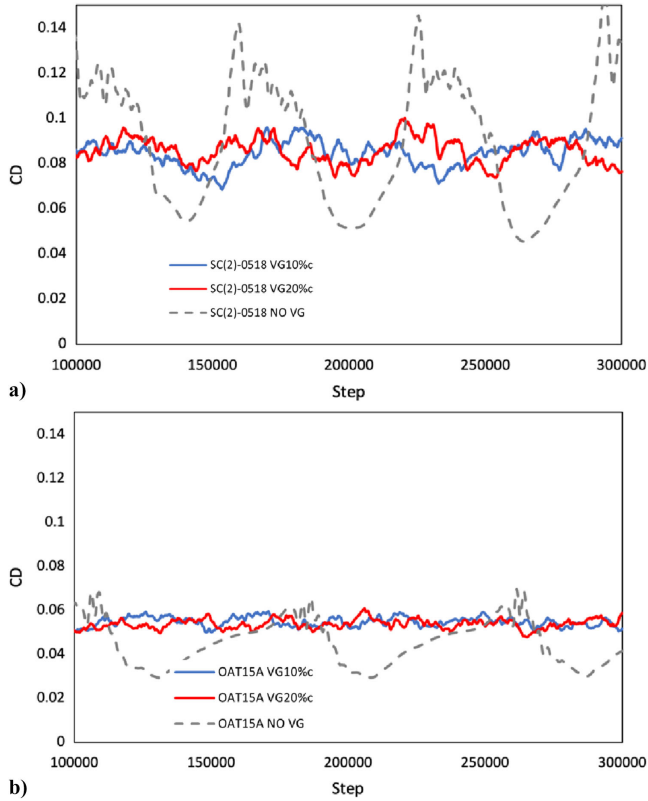
Fig. 13   Drag coefficient time history for VG-equipped cases: a) C_D history for the SC(2)-0518 airfoil and b) C_D history for the OAT15A airfoil. For comparison, the C_D history for cases without VGs is represented with dashed lines.

drag fluctuation with the VGs attached, showing similar trends to the C_L histories. The VG-attached cases resulted in a smaller C_D fluctuation, ranging from 0.07 to 0.10. Compared to the VG-less case with C_D fluctuation in a range of 0.04–0.15, the VGs suppressed the fluctuation by approximately 72.7%. Considering the averaged values, the $10\%c$ VG case resulted in $C_{D,\mathrm{ave}} = 0.0846$ and the $20\%c$ case in $C_{D,\mathrm{ave}} = 0.0857$, with an improvement of 1.3% less drag with the VG at $10\%c$. Considering that $C_{D,\mathrm{ave}}$ was 0.0897 in the VG-less case, applying the VG on the SC(2)-0518 was found to improve C_D by approximately 5%.

The C_D time history of OAT15A with VG is equally shown in Fig. 13b. The C_D time history resembles the C_L history, showing that VGs effectively suppress the aerodynamic lift fluctuation. Clearly, through the entire calculation step, the drag is low compared to that in the SC(2)-0518 cases. From the averaged values, $C_{D,\mathrm{ave}} = 0.0547$ with

VG at $10\%c$, $C_{D,\mathrm{ave}} = 0.0538$ with VG at $20\%c$, and the $20\%c$ VG-attached case shows 1.6% less C_D value. This is different from the SC(2)-0518 case, which showed a lower drag with VG at $10\%c$. Additionally, the C_D of the VG-less case resulted in $C_{D,\mathrm{ave}} = 0.0451$; therefore, by installing the VG, $C_{D,\mathrm{ave}}$ increased significantly by approximately 20%. Although the VGs contribute to increased drag, the advantages associated with mitigating the shock buffet must be carefully weighed.

C.   Pressure Coefficients

The time-averaged C_p distributions are presented in Fig. 14. The C_p values are delineated at the cross section through the tip of the VG ($y = 0$) and averaged over three buffet periods for each airfoil. A pressure perturbation is observed at the location where the VG is positioned, prompted by a pressure rise at the upwind side of the VG and a rapid pressure decrease at the downstream side of the VG.

Examination of the SC(2)-0518 airfoil reveals that, compared to the $20\%c$ case, the $10\%c$ VG case exhibits a consistently lower C_p value in the range of $0.2 \leq x/c \leq 0.4$ on the airfoil upper surface, as shown in Fig. 14a. This contributes to a marginal increase in $C_L(C_{L\mathrm{ave}} = 0.874$ with the VG at $10\%c$ vs $C_{L\mathrm{ave}} = 0.872$ with the VG at $20\%c$), as C_L correlates with the area encompassed by the closed curve in the C_p graph. A similar trend is observed for the OAT15A airfoil (Fig. 14b), where minor variations in C_p according to VG chord length positions are discernible in the vicinity of $0.3 \leq c/c \leq 0.8$ within the wake region of the VG. Compared to the $20\%c$ case, the $10\%c$ VG case exhibits a marginally reduced C_p value, yielding a greater C_L for the $10\%c$ VG configuration ($C_{L\mathrm{ave}} = 1.01$ with VG at $10\%c$ vs $C_{L\mathrm{ave}} = 0.985$ with VG at $20\%c$). Notably, differences in C_p are also evident near the airfoil trailing edge on the lower surface, where the C_p is marginally increased in the region of $0.7 \leq x/c \leq 0.9$ relative to both the $20\%c$ VG and no-VG scenarios.

D.   RMS Fields of Pressure Fluctuation

The RMS fields in the y − plane, P_{rms}, representing P/P_∞, are depicted in Fig. 15. These pressure fluctuations, stemming from the unsteady nature of the shock and turbulent flow, highlight regions of heightened flow variability. For the SC(2)-0518 airfoil without VGs (Fig. 15a), P_{rms} intensifies around $0.15 \leq x/c \leq 0.45$, corresponding to the shock oscillation zone, and near $0.70 \leq x/c$ at the trailing edge of the upper wing surface, indicative of pressure variations from unsteady vortices and complex wake structures. Similarly, the OAT15A airfoil (Fig. 15b) exhibits distinct transonic buffet characteristics, although with disparities in shock wave locations (located more aft around $0.30 \leq x/c \leq 0.55$) and the intricate flowfields at the trailing edges (around $0.90 \leq x/c$). In cases equipped with VGs, the chordwise extent of self-sustained shock oscillation is markedly diminished for both airfoil models, irrespective of the VG chord length placement.
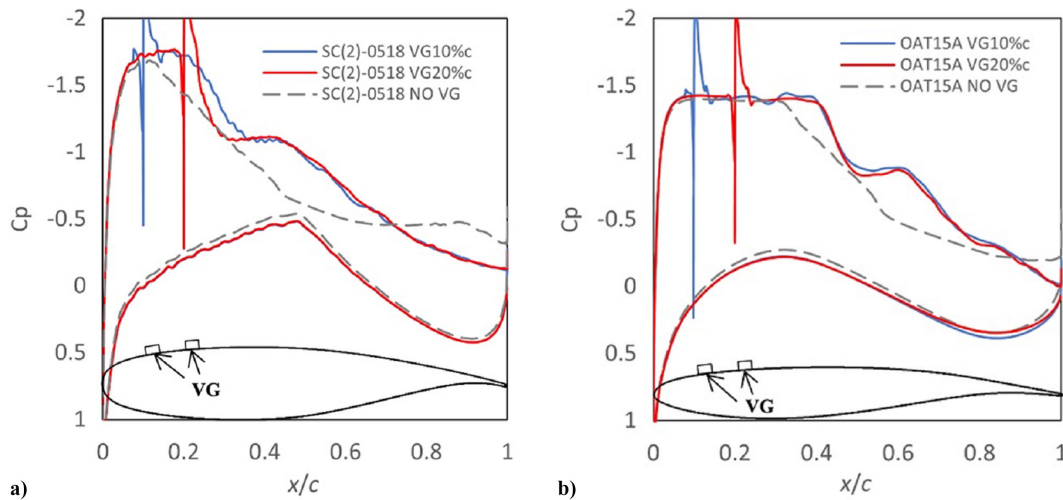

Fig. 14   Time-averaged pressure coefficient distribution around the airfoil with VGs: a) C_p over the SC(2)-0518 airfoil and b) C_p over the OAT15A airfoil.
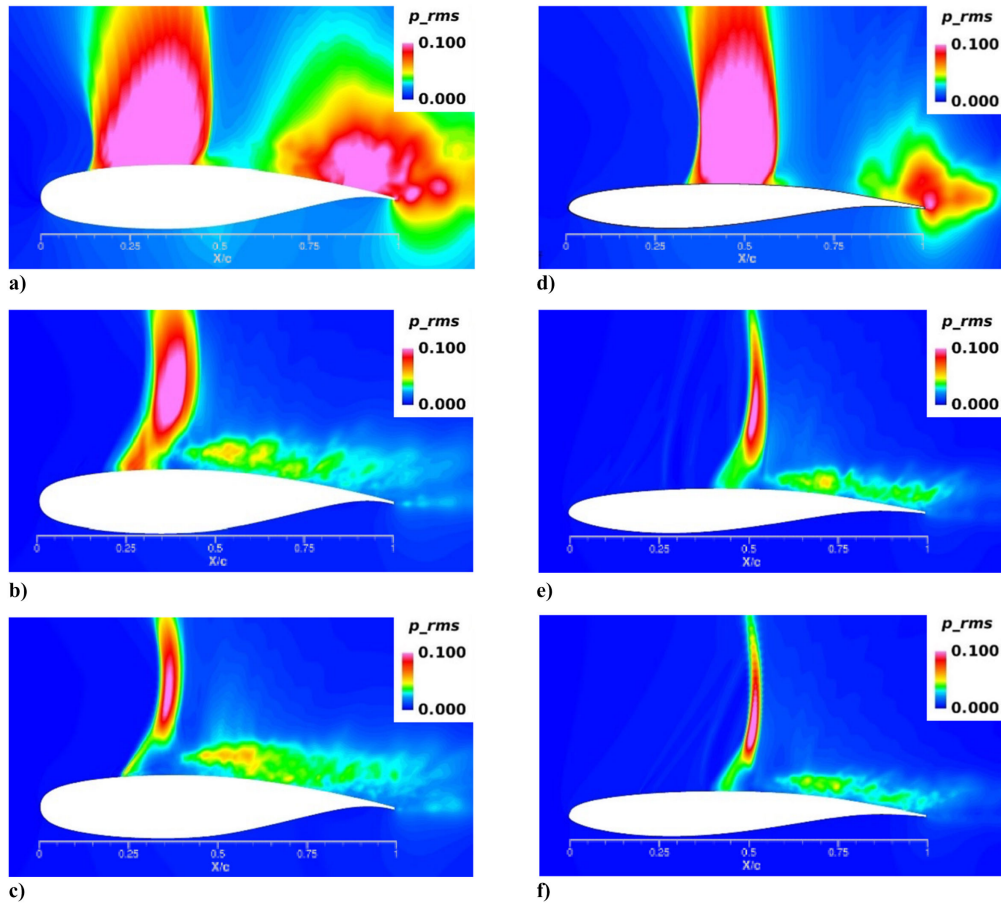
Fig. 15 P_{rms} fields at the cross section $y = 0$. Panels a–c) pertain to SC(2)-0518, whereas d–f) depict OAT15A, with a) and d) representing cases without VGs, b) and e) featuring VGs at $10\%c$, and c) and f) featuring VGs at $20\%c$.

Across all airfoil configurations, VGs contribute two discernible benefits: 1) they attenuate the magnitude of shock wave oscillations, and 2) they suppress the unsteady flows that arise near the trailing edge.

Examination of the SC(2)-0518 airfoil (Figs. 15a–15c) shows that the shock wave oscillations vary with the VG chord length position. The VG at $20\%c$ (Fig. 15c) exhibits more limited chord length fluctuations of the shock wave than the VG placed at $10\%c$ (Fig. 15b). In the latter, the pressure fluctuations are more pronounced near the wing surface in the range of $0.20 \leq x/c \leq 0.40$, suggesting that shock wave oscillations are not as effectively mitigated as in the $20\%c$ VG case. Additionally, the pressure disturbances extend further aft compared to the $20\%c$ placement. Despite an increased lift coefficient, the VG at $10\%c$ does not sufficiently suppress buffeting, which is the primary function expected from VG installation. The pressure fluctuations around

$0.6 \leq x/c$ are likely attributed to unsteady wake vortices instigated by the VG, with marginal differences between the two VG placements.

Parallel observations are noted for the OAT15A airfoil with VGs (Figs. 15d–15f). As with SC(2)-0518, the pressure fluctuation in proximity to the shock wave is broader for the VG positioned at $10\%c$ (Fig. 15e) relative to chord length. The lift coefficient enhancement in the $10\%c$ VG scenario, as delineated in Sec. II.A, results from a more aft shock wave initiation, where boundary-layer separation ensues further downstream, consequently elevating the lift coefficient.

E.   Surface Pressure RMS Fields

Figure 16 depicts the P_{rms} distributions over the upper wing surface, comparing cases with and without VGs. The SC(2)-0518 airfoil
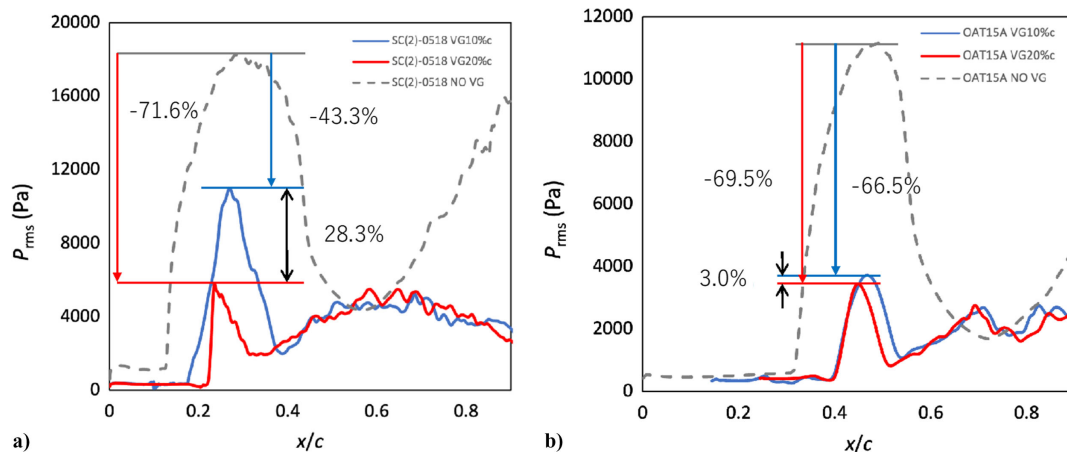

Fig. 16   Surface P_{rms} distributions over the upper wing surface: a) SC(2)-0518 and b) OAT15A.

without VGs (Fig. 16a) showed a higher P_{rms} value than the OAT15A airfoil (Fig. 16b), which is attributed to the stronger shock wave. The impact of VG positions was also significant over SC(2)-0518. The VG at $10\%c$ demonstrated a higher P_{rms} peak value (indicated in blue) than the $20\%c$ placement (shown in red): the P_{rms} was 28.3% lower in the $20\%c$ case, suggesting more effective buffet suppression with the VG placed at $20\%c$. In the $20\%c$ case, a marked increase in P_{rms} was noted at $x/c = 0.20$, where the VG was positioned. This suggests that the shock was constrained from moving further upwind than $x/c = 0.20$ (as indicated by a sharp decrease in P_{rms} from the downwind to the upwind side of the VG), indicating that the shock wave oscillation was dampened by the VG.

In contrast, the difference between the $10\%c$ and $20\%c$ VG-attached OAT15A airfoils was minor. The peak P_{rms} values for both VG placements were nearly identical, with only 3.0% difference. In contrast to SC(2)-0518, the shock on OAT15A oscillated in the range of $0.40 < x/c < 0.55$ (where the P_{rms} was comparatively high); thus, the shock was considerably far from the VG (at $x/c = 0.10$ and 0.20) to be affected by it.

F. Skin Friction Coefficient

The skin friction coefficient C_f distribution is discussed here to evaluate the efficacy of VGs. Figure 17 shows the mean C_f contour plots for each case. Figure 17a shows the VG-attached/unattached cases from SC(2)-0518. In the VG-less case, C_f gradually decreases around $0.15 \leq x/c \leq 0.45$, which coincides with the shock oscillation zone observed in the P_{rms} results, which was discussed earlier. In the two VG-attached cases, the high-C_f zone appears behind the VG, being created from the wake of the VG. Interestingly, the VG chordwise position does not affect the end position of the wake, with both cases ending at $x/c = 0.55$. Although the VG position in the $10\%c$ and $20\%c$ VG-attached cases differs by $10\%c$ in the chordwise direction, the VG wake ends at the same position at $x/c = 0.55$. The OAT15A cases shows a similar trend on the flow characteristics, except that the averaged flow separation is more aft at $0.30 \leq x/c \leq 0.55$, as discussed earlier. Similarly to the SC(2)-0518 with VGs, a parallel characteristic of the VG wake length can be observed after the interference with the shock wave (i.e., boundary-layer separation), which was same for both VG-attached cases.

The differences revealed by these two wing cases are the interference with the airfoil-induced shock wave and the VG. Among the $10\%c$ VG-attached case on SC(2)-0518 and the $10\%c$ and $20\%c$ VG-attached OAT15A cases, the VG is attached upstream of the boundary-layer separation line. The VG-induced wake is generated

at the flow-attached region. However, in the $20\%c$ VG-attached case on the SC(2)-0518 airfoil, the VG interferes with the shock. The VG also creates a shock wave, and the interaction between the VG shock and airfoil-induced shock waves acts as an effective "shock dampener."

G. Q Criterion ($Q = 10^{-4}$) and $M = 1.2$ Isosurface

Figure 18 presents the instantaneous contours of the Q criterion ($Q = 10^{-4}$) and $M = 1.2$ isosurface at the 200,000th calculation step for each airfoil. The non-VG simulations (Figs. 18a and 18d) show quasi-2-D flows in the spanwise direction on the top surface of both wings. In the VG-attached cases (Figs. 18b, 18c, 18e, and 18f), the flow before the shock (on the upwind side) remains quasi-2-D. However, after interacting with the shock wave, the boundary layer disintegrates into smaller, complex, 3-D vortex structures. Large-scale vortex structures are evident between the shock and VG wake. The VG-induced wake vortices diffuse upon interacting with the shock wave, subsequently breaking down into multiple smaller and more complex vortices.

In each VG-attached case (Figs. 18b, 18c, 18e, and 18f), a tube-like wake resulting from the VG extends from its location to the separation point, with the exception of the SC(2)-0518 airfoil with a VG at $20\%c$ (Fig. 18c). In Figs. 18b, 18e, and 18f, the vortex wake remains wall-attached, then diffuses and breaks down into smaller vortices. However, in Fig. 18c, the distinct VG wake observed in the other three scenarios are not discernible. This can be attributed to the boundary-layer separation occurring downstream of the VG. In Fig. 18c, the wake emerges within the separated flow region, leading to its fragmentation into smaller vortices without the formation of the tube-like structure behind the VG.

Examination of the shock isosurfaces reveals that in every VG-attached case, the intersection between the VG wake and the shock isosurface protrudes upstream: The shock deforms and widens as it emanates from the diffused VG wake vortex, forming a distorted shock wave. This process creates a "V"-shaped detachment line, which leads to a supersonic post-shock condition, in contrast to the subsonic state expected behind a normal shock. Although a disparity between the two states is present, it does not escalate to an unstable mode, owing to the intricate and unsteady interactions of shockwaves, the VG, and the VG-induced separated boundary layer observed in this study.

V. Conclusions

Numerical calculations of transonic buffet were performed on two supercritical airfoils, SC(2)-0518 and OAT15A, using Zonal
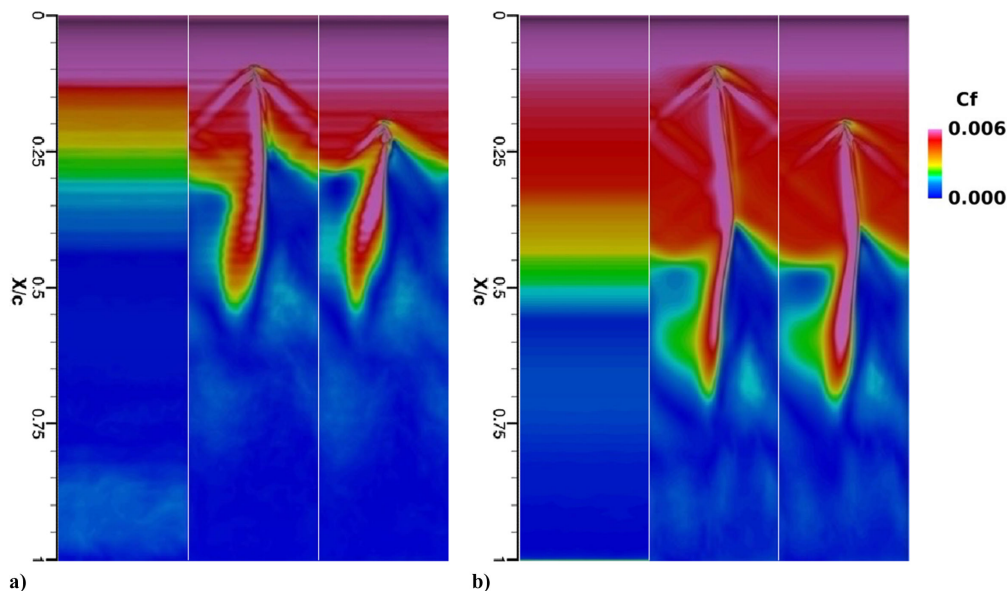

Fig. 17 C_f **distributions on the airfoil in the averaged field: a) SC(2)-0518 and b) OAT15A cases. Both panels represent the VG-unattached, VG at $10\%c$, and VG at $20\%c$ cases, each from left to right.**
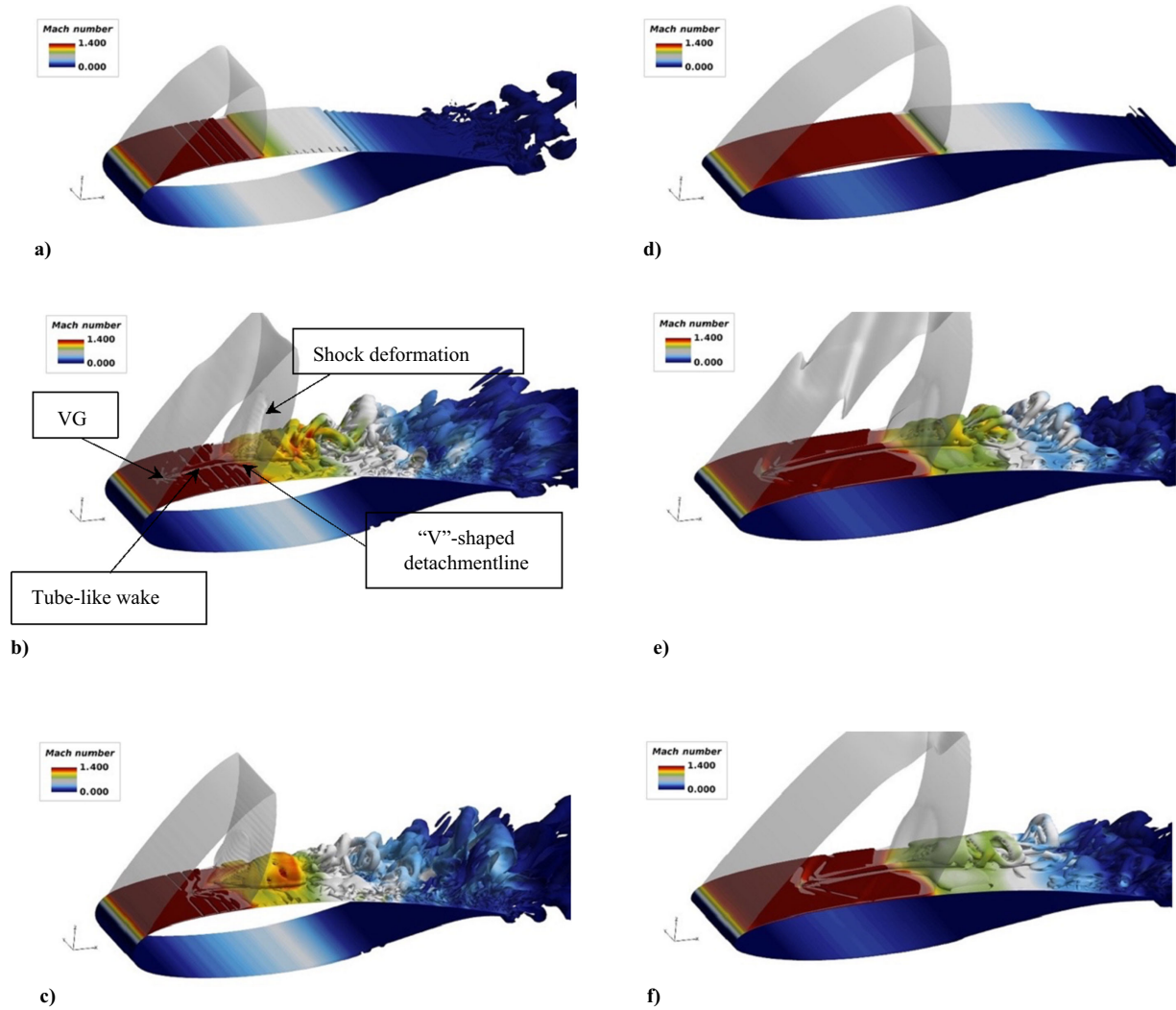
Fig. 18 Q criterion ($Q = 10^{-4}$) and $M = 1.2$ isosurfaces. Panels a–c) pertain to SC(2)-0518, whereas d–f) depict OAT15A, with a) and d) representing cases without VGs, b) and e) featuring VGs at 10%c, and c) and f) featuring VGs at 20%c.

DES to accurately replicate the shock wave buffet phenomenon. VGs were used for the suppression of shock wave oscillations. A parametric study was conducted with blade-type VGs, with their attachment positions on the airfoil at 10% and 20% of the chord length.

Using the numerical calculations on the VG-less airfoils, we successfully reproduced the transonic shock wave buffet, and its oscillation frequencies were consistent with experimental data. The Zonal DES approach—calculating flow in the RANS mode near the wall and in the LES mode outside this region—resolved unsteady, finer flow details more precisely than RANS and with less computational demand than WMLES. The time-averaged pressure coefficient on the airfoil closely agreed with the experimental results.

Application of VGs revealed a suppression effect on the unsteady shock wave oscillations for both airfoils, contributing to transonic buffet suppression. Analysis of the lift coefficient time histories indicated that although small amplitude C_L fluctuations persisted for both airfoil types with VGs attached, the amplitudes of the larger C_L fluctuations were dampened, confirming the effectiveness of the VGs. Additionally, compared to the 20%c cases, a minor increase in C_L was observed in the 10%c VG-attached cases for both airfoils, with a 0.23% increase for SC(2)-0518 and a 2.5% increase for OAT15A.

Visualized pressure RMS results indicated differences in the flow attachment region depending on the chordwise placement of the VGs. With the VGs at 10%c on both airfoils, the shock wave

was positioned further downstream compared to the 20%c-placed VGs, resulting in a longer flow-attachment region (i.e., higher C_L). Specifically, the C_L increase with VGs at 10%c was notable, with a 2.5% improvement over the 20%c-attached cases.

Visualization of the Q criterion and shock wave isosurfaces revealed the formation of a single downstream vortex extending from the VG trailing edge to the shock wave. The interaction between the VG downstream vortex and the shock wave resulted in significant vortex diffusion, creating a complex flowfield. Moreover, in the region where the VG downstream vortex interacted with the shock wave, the shock wave was displaced upstream, leading to the boundary-layer separation moving upstream and the formation of a "V"-shaped flow separation line. The complex interaction between the induced shock wave, VG wake, and the VG led to an effective suppression of shock wave oscillations.

Future work will consider an advanced analysis of the shock-wave/boundary-layer interactions of the transonic buffet when the VG is attached. Understanding the pressure wave propagations around the airfoil is essential owing to the crucial role of pressure wave propagation in explicating the mechanism, by which VGs suppress the transonic buffet. The results we obtained from the Zonal DES calculations will provide more complex data relative to RANS-calculated results; nevertheless, we have to understand the pros and the cons of each turbulence model. Further, based on what we have observed through this research, a further multiparametric study on VG is needed for practical application.

Acknowledgments

References

[1] Lee, B. H. K., "Investigation of Flow Separation on a Supercritical Airfoil," *Journal of Aircraft*, Vol. 26, No. 11, 1989, pp. 1032–1037.
https://doi.org/10.2514/3.45876

[2] Jacquin, L., Molton, P., Deck, S., Maury, B., and Soulevant, D., "Experimental Study of Shock Oscillation over a Transonic Supercritical Profile," *AIAA Journal*, Vol. 47, No. 9, 2009, pp. 1985–1994.
https://doi.org/10.2514/1.30190

[3] Deck, S., "Numerical Simulation of Transonic Buffet over a Supercritical Airfoil," *AIAA Journal*, Vol. 43, No. 7, 2005, pp. 1556–1566.
https://doi.org/10.2514/1.9885

[4] Kouchi, T., Yamaguchi, S., Koike, S., Nakajima, T., Sato, M., Kanda, H., and Yanase, S., "Wavelet Analysis of Transonic Buffet on a Two-Dimensional Airfoil with Vortex Generators," *Experiments in Fluids*, Vol. 57, Oct. 2016, Paper 166.
https://doi.org/10.1007/s00348-016-2261-2

[5] Takimoto, H., "Numerical Study on Suppression of Transonic Buffet by Vortex Generators," Master's Thesis, Yokohama National Univ., Yokohama, Japan, 2020 (in Japanese, unpublished).

[6] Yamaguchi, S., Kouchi, T., Koike, S., Nakajima, T., Sato, M., Kanda, H., and Yanase, S., "Fast-Framing Focusing Schlieren Visualization of Two-Dimensional Wing Buffet," *Journal of the Japan Society for Aeronautical and Space Sciences*, Vol. 63, No. 4, 2015, pp. 166–174.

[7] Tsukamoto, Y., "Numerical Analysis of Vortex-Generators/Wing-Boundary-Layer Interactions for Transonic Buffet Suppression," Bachelor's Thesis, Yokohama National Univ., Yokohama, Japan, 2022 (in Japanese).

[8] Tsukamoto, Y., "Numerical Research on Vortex Generator/Boundary-Layer Interactions over a Supercritical Airfoil," *Proceedings of the 60th Aircraft Symposium, JSASS-5054*, 2022 (in Japanese).

[9] Hilton, W. F., and Fowler, R. G., "Photographs of Shock Wave Movement," National Physical Lab. NPL R&M 2692, 1947.

[10] Crouch, J. D., Garbaruk, A., and Magidov, D., "Predicting the Onset of Flow Unsteadiness Based on Global Instability," *Journal of Computational Physics*, Vol. 224, No. 2, 2007, pp. 924–940.
https://doi.org/10.1016/j.jcp.2006.10.035

[11] Crouch, J. D., Garbaruk, A., and Strelets, M., "Global Instability in the Onset of Transonic-Wing Buffet," *Journal of Fluid Mechanics*, Vol. 881, Oct. 2019, pp. 3–22.
https://doi.org/10.1017/jfm.2019.748

[12] Paladini, E., Beneddine, S., Dandois, J., Sipp, D., and Robinet, J. C., "Transonic Buffet Instability: From Two-Dimensional Airfoils to Three-Dimensional Swept Wings," *Physical Review Fluids*, Vol. 4, No. 10, 2019, Paper 103906.
https://doi.org/10.1103/PhysRevFluids.4.103906

[13] Moise, P., Zauner, M., Sandham, N. D., Timme, S., and He, W., "Transonic Buffet Characteristics Under Conditions of Free and Forced Transition," *AIAA Journal*, Vol. 61, No. 3, 2023, pp. 1061–1076.
https://doi.org/10.2514/1.J062362

[14] Bartels, R., and Bartels, R., "Computation of Shock Buffet Onset for a Conventional and Supercritical Airfoil," *35th Aerospace Sciences Meeting and Exhibit*, AIAA Paper 1997-0833, 1997.
https://doi.org/10.2514/6.1997-833

[15] Brunet, V., "Computational Study of Buffet Phenomenon with Unsteady RANS Equations," AIAA Paper 2003-3679, 2003.
https://doi.org/10.2514/6.2003-3679

[16] Ishiko, K., Hashimoto, A., Aoyama, T., and Takekawa, K., "Detached-Eddy Simulation of NASA-CRM Transonic Buffet," *Proceedings of the 6th European Conference on Computational Fluid Dynamics (ECFD VI)*, International Center for Numerical Methods in Engineering, Barcelona, Spain, July 2014.

[17] Menter, F., Kuntz, M., and Bender, R., "A Scale-Adaptive Simulation Model for Turbulent Flow Predictions," AIAA Paper 2003-0767, 2003.
https://doi.org/10.2514/6.2003-767

[18] Ehrle, M., Waldmann, A., Lutz, T., and Krämer, E., "Simulation of Transonic Buffet with an Automated Zonal DES Approach," *CEAS Aeronautical Journal*, Vol. 11, Sept. 2020, pp. 1025–1036.
https://doi.org/10.1007/s13272-020-00466-7

[19] Kusunose, K., and Yu, N. J., "Vortex Generator Installation Drag on an Airplane Near Its Cruise Condition," *Journal of Aircraft*, Vol. 40, No. 6, 2003, pp. 1145–1151.
https://doi.org/10.2514/2.7203

[20] Koike, S., Ito, Y., Kusunose, K., Nakajima, T., Sato, M., Kanda, H., Murayama, M., Nakakita, K., and Yamamoto, K., "Effect of Vortex Generators on Two-Dimensional Wings in Transonic Flows," JAXA Research and Development Rept. JAXA-RR-14-002, 2014.

[21] Hashimoto, A., Murakami, K., Aoyama, T., Ishiko, K., Hishida, M., Sakashita, M., and Lahur, P., "Toward the Fastest Unstructured CFD Code 'FaSTAR'," AIAA Paper 2012-1075, 2012.
https://doi.org/10.2514/6.2012-1075

[22] Hashimoto, A., Ishida, T., Aoyama, T., Ohmichi, Y., Yamamoto, T., and Hayashi, K., "Current Progress in Unsteady Transonic Buffet Simulation with Unstructured Grid CFD Code," AIAA Paper 2018-0788, 2018.
https://doi.org/10.2514/6.2018-0788

[23] Van Leer, B., "Towards the Ultimate Conservative Difference Scheme. V. A Second-Order Sequel to Godunov's Method," *Journal of Computational Physics*, Vol. 32, No. 1, 1979, pp. 101–136.
https://doi.org/10.1016/0021-9991(79)90145-1

[24] Shima, E., and Kitamura, K., "Parameter-Free Simple Low-Dissipation AUSM-Family Scheme for All Speeds," *AIAA Journal*, Vol. 49, No. 8, 2011, pp. 1693–1709.
https://doi.org/10.2514/1.J050905

[25] Shima, E., Kitamura, K., and Fujimoto, K., "New Gradient Calculation Method for MUSCL Type CFD Schemes in Arbitrary Polyhedra," AIAA Paper 2010-1081, 2010.
https://doi.org/10.2514/6.2010-1081

[26] Hishida, M., Hashimoto, A., Murakami, K., and Aoyama, T., "A New Slope Limiter for Fast Unstructured CFD Solver FaSTAR," *JAXA Special Publication: Proceedings of 42nd Fluid Dynamics Conference/ Aerospace Numerical Simulation Symposium*, JAXA-SP-10-012, Japan Aerospace Exploration Agency, Tokyo, Japan, 2010, pp. 85–90 (in Japanese).

[27] Sharov, D., and Nakahashi, K., "Reordering of Hybrid Unstructured Grids for Lower-Upper Symmetric Gauss-Seidel Computations," *AIAA Journal*, Vol. 36, No. 3, 1998, pp. 484–486.
https://doi.org/10.2514/2.392

[28] Visbal, M. R., and Gordnier, R. E., "A High-Order Flow Solver for Deforming and Moving Meshes," AIAA Paper 2000-2619, 2000.
https://doi.org/10.2514/6.2000-2619

[29] Tucker, P. G., *Advanced Computational Fluid and Aerodynamics*, Cambridge Aerospace Series, Cambridge Univ. Press, Cambridge, England, U.K., 2016, p. 268.
https://doi.org/10.1017/CBO9781139872010

[30] Ishida, T., Ishiko, K., Hashimoto, A., Aoyama, T., and Takekawa, K., "Transonic Buffet Simulation over Supercritical Airfoil by Unsteady-FaSTAR Code," AIAA Paper 2016-1310, 2016.
https://doi.org/10.2514/6.2016-1310

[31] Shur, M. L., Spalart, P. R., Strelets, M. K., and Travin, A. K., "A Hybrid RANS-LES Approach with Delayed-DES and Wall-Modelled LES Capabilities," *International Journal of Heat and Fluid Flow*, Vol. 29, No. 6, 2008, pp. 1638–1649.
https://doi.org/10.1016/j.ijheatfluidflow.2008.07.001

[32] Wang, Z. N., and Tucker, P. G., "Hierarchical Turbulence and Geometry Modeling: Case Study for Fan Stage Flows," *AIAA Journal*, Vol. 61, No. 7, 2023, pp. 2824–2839.
https://doi.org/10.2514/1.J062495

[33] Renard, N., and Deck, S., "Improvements in Zonal Detached Eddy Simulation for Wall Modeled Large Eddy Simulation," *AIAA Journal*, Vol. 53, No. 11, 2015, pp. 3499–3504.
https://doi.org/10.2514/1.J054143

[34] Spalart, P., and Allmaras, S., "A One-Equation Turbulence Model for Aerodynamic Flows," *30th Aerospace Sciences Meeting and Exhibit*,

AIAA Paper 1992-0439, 1992.
https://doi.org/10.2514/6.1992-439

[35] Husson, J., Terracol, M., Deck, S., and Le Garrec, T., "A Comprehensive Framework for Robust Hybrid RANS/LES Simulations of Wall-Bounded Flows in LMB," *Journal of Computational Physics*, Vol. 502, April 2024, Paper 112814.
https://doi.org/10.1016/j.jcp.2024.112814

[36] Deck, S., Weiss, P.-É., Pamiès, M., and Garnier, E., "Zonal Detached Eddy Simulation of a Spatially Developing Flat Plate Turbulent Boundary Layer," *Computers and Fluids*, Vol. 48, No. 1, 2011, pp. 1–15.
https://doi.org/10.1016/j.compfluid.2011.03.009

[37] Harris, C. D., "NASA Supercritical Airfoils: A Matrix of Family-Related Airfoils," NASA TP-2969, 1990.

[38] "Extrude," Pointwise, https://www.pointwise.com/doc/user-manual/create/extrude/ [retrieved 19 Dec. 2023].

S. Ricci
Associate Editor